RESEARCH ARTICLE

NANO · MICRO small
www.small-journal.com

Temperature-Dependent Surface Anisotropy in (110) Epitaxial Rare Earth Iron Garnet Films

Yixuan Song, Katharina Lasinger, Hao Tang, Ju Li, Geoffrey S. D. Beach, and Caroline A. Ross**

Ferrimagnetic oxide thin films are important material platforms for spintronic devices. Films grown on low symmetry orientations such as (110) exhibit complex anisotropy landscapes that can provide insight into novel phenomena such as spin-torque auto-oscillation and spin superfluidity. Using spin-Hall magnetoresistance measurements, the in-plane (IP) and out-of-plane (OOP) uniaxial anisotropy energies are determined for a thickness series (5–50 nm) of europium iron garnet (EuIG) and thulium iron garnet (TmIG) films epitaxially grown on a gadolinium gallium substrate with (110) orientation and capped with Pt. Pt/EuIG/GGG exhibits an (001) easy plane of magnetization perpendicular to the substrate, whereas Pt/TmIG/GGG exhibits an (001) hard plane of magnetization perpendicular to the substrate with an IP easy axis. Both IP and OOP surface anisotropy energies comparable in magnitude to the bulk anisotropy are observed. The temperature dependence of the surface anisotropies is consistent with first-order predictions of a simplified Néel surface anisotropy model. By taking advantage of the thickness and temperature dependence demonstrated in these ferrimagnetic oxides grown on the low symmetry (110) orientations, the complex anisotropy landscapes can be tuned to act as a platform to explore rich spin textures and dynamics.

1. Introduction

Magnetic thin films and heterostructures are important material platforms for a range of technological applications including magnetic tunnel junctions in magnetic random-access memory,[1,2] spin-torque oscillators,[3] racetrack memory,[4] magnonic devices,[5] and more. Recently, oxide-based spintronics has raised interest with recent developments focusing on ferrimagnetic and antiferromagnetic oxides and multiferroics.[6–13] Iron garnets (IGs, $R_3Fe_5O_{12}$ where R is a lanthanide, Y or Bi) are ferrimagnetic oxides that show the potential benefits of ultra-fast dynamics for fast current-driven and optical switching,[9] low damping for efficient magnon propagation,[10,11] and reduced power consumption because of current confinement within the charge-to-spin conversion layer. Further, the spin-orbit coupling (SOC) in rare earth IGs (REIGs) also offers opportunities to explore exotic physical phenomena including antisymmetric exchange interaction,[12] chiral spin textures,[13] and orbital current transport and switching.[14] Demonstrating these promising functionalities in REIGs relies on the engineering of appropriate anisotropy landscapes which vary significantly with the choice of rare-earth (including Y) and other elements such as Bi. Perpendicular magnetic anisotropy achieved through strain engineering in epitaxial films of europium iron garnet ($Eu_3Fe_5O_{12}$ or EuIG), thulium iron garnet ($Tm_3Fe_5O_{12}$ or TmIG), terbium iron garnet ($Tb_3Fe_5O_{12}$ or TbIG), and Bi-substituted yttrium iron garnet ($Y_3Fe_5O_{12}$ or YIG)[15–17] allowed for the demonstration of spin-orbit torque (SOT) switching,[18] the study of interfacial Dzyaloshinskii-Moriya interaction (DMI),[12] and SOT-driven domain wall motion.[19]

Epitaxial thin film growth techniques allow precise control and engineering of crystal symmetry. While films are conventionally grown on substrate crystal orientations with high symmetry such as C_4 on (100) or C_3 on (111) to obtain isotropic electronic, magnetic, and optical properties within the film plane,[20] films with low crystal symmetry have raised interest. A lower crystal symmetry, C_2 on (110), has been predicted and demonstrated to be an essential criterion for a wide range of novel spin textures and spin dynamics. For example, antiskyrmions

Y. Song, K. Lasinger, H. Tang, J. Li, G. S. D. Beach, C. A. Ross
Department of Materials Science and Engineering
Massachusetts Institute of Technology
Cambridge, Massachusetts 02139, USA
E-mail: gbeach@mit.edu; caross@mit.edu
K. Lasinger
Department of Materials
ETH Zurich
Zurich CH-8093, Switzerland
J. Li
Department of Nuclear Science and Engineering
Massachusetts Institute of Technology
Cambridge, Massachusetts 02139, USA

The ORCID identification number(s) for the author(s) of this article can be found under https://doi.org/10.1002/smll.202407381

DOI: 10.1002/smll.202407381

rely on anisotropic DMI,[21] and spin-torque auto-oscillation and spin superfluidity require systems with vertical easy-plane anisotropy.[22–25] The SOT switching of in-plane (IP) magnetization, which provides a field-free alternative to the SOT switching of perpendicular magnetization,[26] also requires an IP symmetry breaking (C_2) to stabilize distinct IP states.

Oxide surfaces and interfaces play a critical role in controlling the properties of epitaxial thin films since the total film thickness is typically only at the nanometer scale. Atoms at surfaces and interfaces experience a bonding environment different from the bulk. Consequently, surfaces and interfaces exhibit distinct structural, chemical, electronic, and magnetic properties when compared to the bulk material.[27,28] In the realm of magnetic materials, magnetic anisotropy is a crucial physical property that dictates the magnetization orientation at equilibrium, the dynamic response, and the critical length scales of magnetic textures. Due to inversion symmetry breaking at surfaces and interfaces, the surface layer of atoms can contribute to an additional magnetic anisotropy, termed magnetic surface anisotropy.[29] While this contribution to anisotropy has been well studied for high symmetry orientations,[30–35] oxide surfaces on the low symmetry (110) orientation remain poorly explored.

Here, using spin-Hall magnetoresistance (SMR) measurements, we compare the thickness dependence of the anisotropy energy for EuIG, TmIG, and YIG epitaxially grown on the (110) orientation of gadolinium gallium garnet substrates ($Gd_3Ga_5O_{12}$ or GGG) by pulsed laser deposition (PLD) and capped with Pt. The rare-earth ions Eu^{3+}, Tm^{3+}, and Y^{3+} correspond to a strong SOC with a large magnetoelastic coefficient, a strong SOC with a small magnetoelastic coefficient, and a weak SOC with a small magnetoelastic coefficient, respectively.[36] These three rare-earth substitutions form an informative dataset for comparison. In both EuIG and TmIG films, we observed a strong IP surface anisotropy, comparable in magnitude to the bulk anisotropy energies, while a negligible IP surface and bulk anisotropy was present in YIG films. With density functional theory (DFT) calculations, we determined the atomic configurations for the lowest energy surface, which shows a C_2 symmetry. This symmetry allows both an IP and an out-of-plane (OOP) surface anisotropy contribution, denoted as $K_{\mathrm{IP,\,surface}}$ and $K_{\mathrm{OOP,\,surface}}$, respectively. A set of temperature-dependent measurements shows that both the surface and bulk anisotropy contributions decrease with increasing temperature, consistent with the Néel surface anisotropy model. The demonstration of complex anisotropy landscapes tunable by film thickness and temperature provides an important stepping-stone for spintronic device engineering and spin dynamics investigations.

2. Surface Anisotropy Model

In Néel's surface anisotropy model,[29] missing bonds and therefore magnetic pair interaction terms at the surface naturally give rise to a layer of atoms that contribute to a total anisotropy energy differently from those in the bulk. The magnetic pair interaction energy between atoms $w(r, \psi)$ is expanded in Legendre polynomials:[29,32]

$$w(r,\psi) = G(r) + L(r)\left(\cos^2\psi - \frac{1}{3}\right) + Q(r)\left(\cos^4\psi - 6/7\cos^2\psi - 3/35\right) + \cdots \quad (1)$$

The interaction energy depends on ψ, the angle between the bond axis and the magnetization vector $\boldsymbol{M}$, and on the distance between the pair of atoms r. The first term is spatially isotropic, e.g. magnetic exchange $E_{\mathrm{ex}} = -J_{ij}S_i \cdot S_j$ and does not contribute to the anisotropy. The second, dipolar term describes anisotropies with a twofold symmetry. The third, quadrupolar term describes anisotropies of cubic symmetry. The dipolar term typically dominates over the quadrupolar term. The magnetic anisotropy of a single crystal film can then be calculated by summing up this interaction energy for all nearest-neighbor pairs of atoms in the film.

Strain can be present in an epitaxial thin film because of the lattice mismatch between the film and the substrate. We consider a coordinate system with $\boldsymbol{a}_1$ and $\boldsymbol{a}_2$ describing the direction vectors within the film plane and $\boldsymbol{a}_3$ is the film normal. With the strain tensor defined in Equation. (2), where a uniform strain of $e_0 = (a_{\mathrm{substrate}} - a_{\mathrm{film}})/a_{\mathrm{film}}$ within the film is assumed, and ν denotes the Poisson ratio, the strained bond length and bond axis can be calculated and propagated into the interaction energy. The coefficient for the dipolar term in Equation (1) can be approximated with the first-order Taylor's expansion of $L(r)$ about the unstrained bond length $L(r) = L(r_0) + (\vec{r}_0 \cdot e \cdot \vec{r}_0)\frac{dL}{dr}|_{r_0}$.

$$e = \begin{pmatrix} e_{11} & e_{12} & e_{13} \\ e_{21} & e_{22} & e_{23} \\ e_{31} & e_{32} & e_{33} \end{pmatrix} = e_0 \begin{pmatrix} 1 & 0 & 0 \\ 0 & 1 & 0 \\ 0 & 0 & \frac{-2\nu}{1-\nu} \end{pmatrix} \quad (2)$$

Symmetry arguments show that a threefold or higher rotation axis is required to ensure isotropic properties in the plane normal to that axis.[20] Conversely, the symmetry at the surface of a (110) film plane in a cubic structure reduces to C_{2v}. The symmetry breaking, illustrated with the ball and stick model in **Figure 1**a,b is essential to give rise to both an IP and OOP surface anisotropy in a system with a cubic structure. An OOP surface anisotropy contribution arises from the inversion symmetry breaking at the surface and an IP surface anisotropy contribution arises from the asymmetry between [001] and [$\bar{1}$10] directions on a (110) surface. Analysis using Néel's surface anisotropy approach quantifies the surface contribution to both IP and OOP anisotropy, represented by $K_{\mathrm{IP,\,surface}}$ and $K_{\mathrm{OOP,\,surface}}$, respectively.[32,33] This was also confirmed in experiments.[34] The IP anisotropy $K_{\mathrm{IP,\,surface}}$ is expected to be large due to the presence of a zeroth order $L(r_0)$ term, which for a centrosymmetric system is compensated in the bulk. For a (110) film the surface anisotropy can be written as Equation (3), with the coordinate system being defined as $\mathbf{a}_1 = [\bar{1}10]$, $\mathbf{a}_2 = [001]$ and $\mathbf{a}_3 = [110]$:

$$K_{110,\,\mathrm{surface}} = \left(\frac{1}{2}L(r_0) - e_0 L(r_0)\right)\cos^2\theta + \left(\frac{1}{2}L(r_0) + e_0 L(r_0)\right)\cos^2\phi\sin^2\theta \quad (3)$$

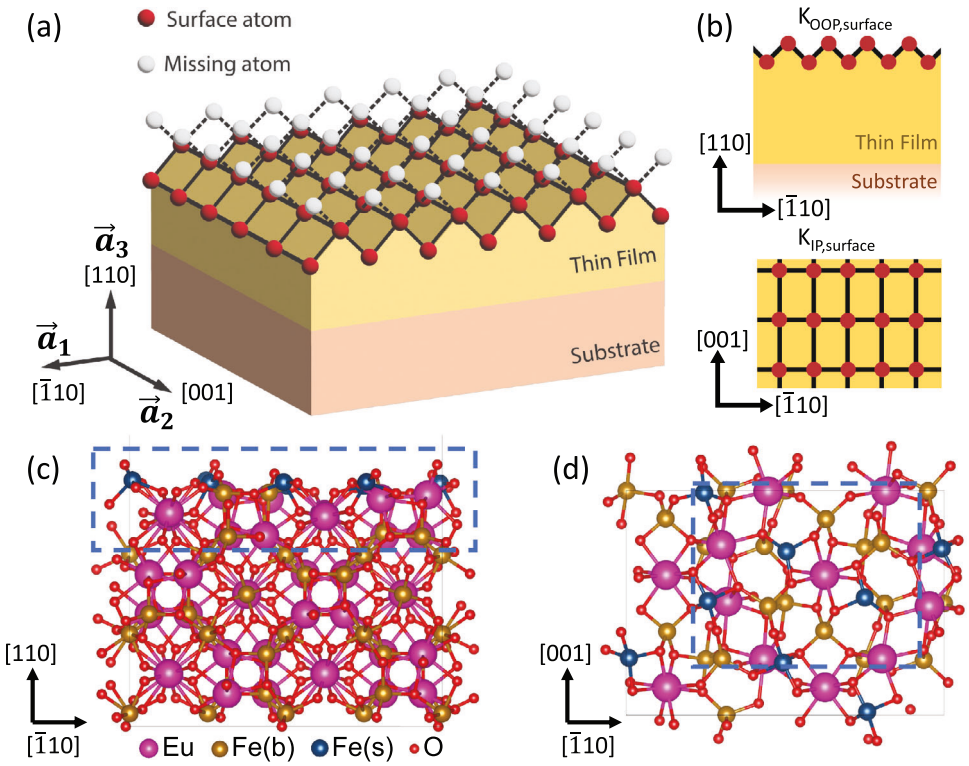

Figure 1. (110) surface schematics in simple cubic structure and garnet structure. a) Schematic of the surface layer of atoms (red sphere) and missing atoms (white sphere), preserved bonds (solid black line), and broken bonds (dashed black line) on a (110) surface for a general picture of a thin film with a simple cubic structure. b) Top: a cross-section view of the (110) surface of a simple cubic structure along [001]. Bottom: a top view of the (110) surface of a simple cubic structure. Two essential symmetry breaking elements result from the broken bonds, namely, an out-of-plane inversion symmetry broken by the surface which gives rise to $K_{OOP,surface,}$ and a 2-fold rotation symmetry on the (110) surface which gives rise to $K_{IP,surface}$. c) A cross-section view of the lowest energy surface in EuIG/GGG (110) determined from DFT calculations, with bulk Fe (b) and surface Fe (s) identified. d) A top view of the (110) surface. Only atoms in the boxed layers of (c) are shown. Atoms in the boxed region of (d) show a 2-fold rotation symmetry including the surface layer of atoms.

where θ and ϕ are angles in spherical polar coordinates in ($\boldsymbol{a}_1$,$\boldsymbol{a}_2$,$\boldsymbol{a}_3$) space. This yields $K_{\mathrm{IP,\,surface}} = \frac{1}{2}L(r_0) + e_0L(r_0)$ and $K_{\mathrm{OOP,\,surface}} = 2e_0L(r_0)$.

3. Results

To elucidate the surface and bulk anisotropy in REIGs, we grew a thickness (t) series of EuIG (t = 5, 8, 14, 21, 26, 37, 43, 45, 53 nm) epitaxially on the (110) orientation of GGG and a thickness series of TmIG (t = 5, 12, 28 nm) on the same substrate and orientation using PLD. Yttrium iron garnet ($Y_3Fe_5O_{12}$ or YIG) of (t = 8, 12, 32 nm) was grown for comparison.

The garnet structure is cubic, $Ia\bar{3}d$, with 8 formula units within the unit cell. The atomic configuration and surface energy of the EuIG and TmIG (110) surfaces are calculated by spin-unrestricted DFT, discussed in Note S6 (Supporting Information) (Supplementary includes references).[37–41] The atomic configuration shown in Figure 1c,d gives the lowest surface energy density for both TmIG and EuIG and is therefore thermodynamically favorable. This lowest energy surface has a Fe termination with no RE atoms in the top layer. Since the Fe-O bond is lower in energy compared to the RE-O bond, this surface termination has the lowest energy. The top view of the surface atoms shown in Figure 1d illustrates the two-fold symmetry of the lowest energy surface which allows for an IP anisotropy.

Film thickness and strain were determined through high-resolution X-ray diffraction (HR-XRD) measurements (**Figure** 2a,b). Both HR-XRD and reciprocal space mapping (RSM) measurements (Note S1, Supporting Information) showed negligible strain relaxation within the error bar, indicated by the consistent OOP strain as a function of thickness plotted in Figure 2c,d. The effect of strain variations between samples on the anisotropy extraction is discussed in Note S3 (Supporting Information). Using vibrating sample magnetometry (VSM) measurements with a field applied along the easy anisotropy axis ([110] for EuIG and [001] for TmIG), we determined the saturation magnetization (M_s) for all film thicknesses (Figure 2e,f). The bulk saturation magnetization ($M_{s,0}$) and a magnetic dead layer (t_0), which does not contribute magnetically to the film, are determined (Methods) to be 77 ± 1 kA/m and 2.9 ± 0.4 nm for EuIG and 98 ± 6 kA m^{-1} and 2.0 ± 0.1 nm for TmIG, respectively (Figure 2g,h). The bulk saturation magnetization is lower than the values reported for bulk crystals (at room temperature, 93 kA m^{-1} for EuIG and 111 kA m^{-1} for TmIG)[42] which may be a result of nonideal cation stoichiometry or oxygen content in thin films.[43] The dead layer likely originates from interdiffusion at the substrate which occurs over a distance of

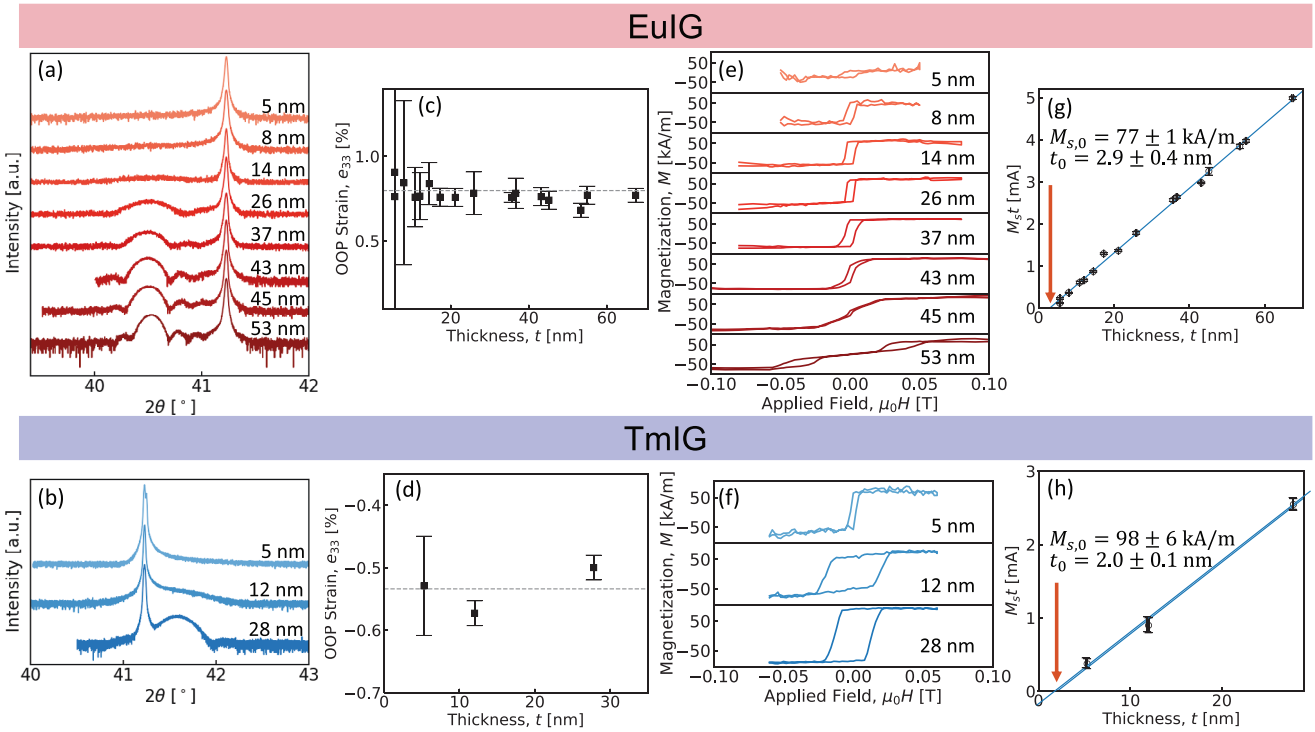

Figure 2. Sample characterization of the thickness series for EuIG/GGG (110) (top) and for TmIG/GGG (110) (bottom). a,b) HR-XRD measurements around the (440) reflection. 2θ scans reveal progressively more distinct film peaks and Laue fringes as the film thickness increases. The film peak position and Laue fringes were fitted to extract lattice spacing, film thickness, and composition. c,d) OOP strain calculated from OOP lattice spacing obtained via HRXRD. Error bars on thinner films are larger due to higher uncertainty in the fits of less pronounced film peaks. The dashed line marks the average. e,f) VSM measurements with field applied along the respective easy axes [110] ([001]) EuIG (TmIG). g,h) Bulk saturation magnetization $M_{s,0}$ and dead layer thickness t_0 are extracted from the measured saturation magnetization M_s of the individual films with thickness t through Eq. M1.

order 1 nm;[12] the room temperature Pt sputtering after breaking vacuum leads to little interdiffusion.[44] The evolution from a square hysteresis loop in the thinner EuIG to a sheared double hysteresis loop in the thicker EuIG is a result of the transition in the lowest energy anisotropy axis from [110] to [$\bar{1}$10] together with a magnetocrystalline anisotropy which creates a four-fold symmetric energy barrier.[45] With atomic force microscopy (Figure S8, Supporting Information), we determined a surface roughness of 0.3 nm which varies little with thickness.

SMR measurements were performed to accurately determine the anisotropy energies along the principal axes, $\boldsymbol{a}_1$ = [$\bar{1}$10], $\boldsymbol{a}_2$ = [001] and $\boldsymbol{a}_3$ = [110] (Methods). With the device stack Pt (4 nm)/REIG (t nm)/GGG (110), where RE = [Eu, Tm, Y], and the device geometry shown in **Figure 3a**, we measured the transverse Hall voltage as a function of an applied field. A change in the equilibrium magnetization vector in the REIG by an external field alters the spin reflectivity at the Pt/REIG interface and manifests as a variation in the transverse charge accumulation through the inverse spin-Hall effect.[46,47] Typical SMR curves are shown in Figure 3b for EuIG and Figure 3c for TmIG. The measured transverse Hall voltage is converted to resistance (R_H) by normalizing against the current I = 0.5 mA and plotted against the field applied along the three principal axes. SMR for the lowest energy axis shows a minimal variation in R_H with the applied field, while higher energy anisotropy axes show a continuous evolution with the applied field until the magnetization is saturated at the effective anisotropy field H_k.

Four different anisotropy landscapes were observed over the thickness and temperature range investigated in this study, shown schematically in Figure 3b,c. They are an OOP easy-plane (OPEP) for EuIG with the lowest energy axis along s[110] (top panel in Figure 2b) or [$\bar{1}$10] (bottom panel in Figure 3b), and an OOP hard-plane (OPHP) for TmIG with the highest energy axis along [$\bar{1}$10] (top panel in Figure 3c) or [110] (bottom panel in Figure 2c). These anisotropy landscapes arise from the interplay of magnetostatic, magnetoelastic, magnetocrystalline, growth-induced, and surface anisotropies,[42,48–50] and lead to domain patterns with IP anisotropy, specifically stripe domains in EuIG and the domain wall characters evolves with changing film thicknesses (Figure S7, Supporting Information). The magnetoelastic contribution to the anisotropy landscape of EuIG and TmIG is a dominant factor and differs between the two material systems due to their different strain states (tensile in the plane for TmIG, compressive for EuIG) and dissimilar magnetoelastic coefficients λ. At room temperature $\lambda_{100} = 21 \times 10^{-6}$ and $\lambda_{111} = 1.8 \times 10^{-6}$ for EuIG and $\lambda_{100} = 1.4 \times 10^{-6}$ and $\lambda_{111} = -5.2 \times 10^{-6}$ for TmIG.[42]

Figure 4a,b shows the plot of extracted anisotropy energies against $1/(t - t_0)$ for EuIG and TmIG, respectively, where t is the film thickness determined by HR-XRD and t_0 is the extracted dead layer thickness (Methods B and Note S1,

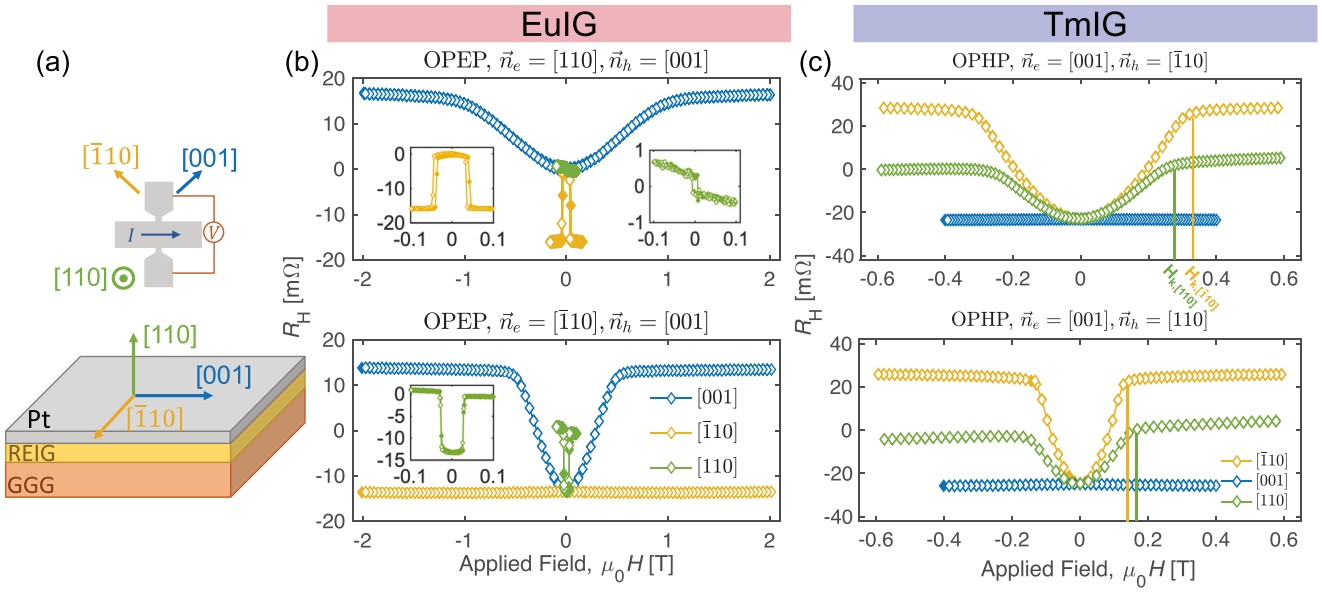

Figure 3. SMR measurement schematics and representative dataset for EuIG and TmIG. a) Schematics of the device geometry (top) for SMR measurements and the film stack (bottom). The current is aligned 45° from the IP anisotropy axes [001] and [$\bar{1}$10]. Film normal is along [110]. b) Example SMR measurements for Pt/EuIG (45 nm)/GGG (110) at − 30 °C (top) and 30 °C (bottom). The OPEP anisotropy landscape changes from having the easiest axis along [110] at − 30 °C to along [$\bar{1}$10] at 30°C. c) Pt/TmIG (5 nm)/GGG (110) at − 50 °C (top) and 50 °C (bottom). The OPHP anisotropy landscape changes from having the hardest axis along [$\bar{1}$10] at − 50 °C to [110] at 50 °C .

Supporting Information). We define the IP anisotropy energy density as $K_{IP} = E[001] - E[\bar{1}10]$ and the OOP anisotropy energy density as $K_{OOP} = E[110] - E[\bar{1}10]$. A clear $1/t$ dependence is observed in the IP anisotropy (K_{IP}) for both EuIG and TmIG over the thickness range. The OOP anisotropy (K_{OOP}) shows a $1/t$ dependence for TmIG. This trend is less clear for EuIG because the larger K_{IP} values propagate larger percentage errors to the relatively small K_{OOP}, which obscures any expected trend. Similar measurements were performed for the YIG thickness series.

We extract the surface and bulk contribution to the IP and OOP anisotropy by fitting to Equation (4) and Equation (5):

$$K_{IP} = K_{IP,bulk} + \frac{E_{IP,surface}}{t - t_0} = K_{IP,bulk} + \frac{K_{IP,surface} \cdot h}{t - t_0} \quad (4)$$

$$K_{OOP} = K_{OOP,bulk} + \frac{E_{OOP,surface}}{t - t_0} = K_{OOP,bulk} + \frac{K_{OOP,surface} \cdot h}{t - t_0} \quad (5)$$

where $K_{IP(OOP),bulk}$ is the bulk IP (OOP) anisotropy volume density and $E_{IP(OOP),surface}$ is the surface IP (OOP) anisotropy area density. The extracted anisotropy energies are summarized in **Table 1**. To provide a convenient comparison between bulk and surface anisotropy values, we convert the surface anisotropy area density to volume density using the relation, $E_{IP(OOP),surface} = K_{IP(OOP),surface} \cdot h$, where h is the thickness of surface atoms contributing to the surface anisotropy. We approximate h by the diagonal length of one unit cell (twice the (110) plane spacing), i.e., $h = a(1 + e_{33})\sqrt{2}$, where a is the lattice parameter and e_{33} is the OOP strain component. Since our choice of h is likely an overestimation of the depth of atoms affected by the free surface, $K_{IP(OOP),surface}$ represents a lower bound for its actual value.

Having established a clear signature of surface anisotropy, we explored the temperature dependence of both the surface and bulk anisotropies by performing temperature-dependent SMR measurements for selected thicknesses of EuIG and all thicknesses of TmIG over the temperature range of 220 to 320 K. Figure 4c,d show examples of the temperature dependence of the extracted anisotropy values. Monotonic dependences on temperature were found for both a thin and thick film with slightly different gradients. (The complete data set is available in Note S4, Supporting Information). We observed a transition in the easiest (hardest) anisotropy axis in EuIG (TmIG) at T_{EPT} (T_{HPT}). In other words, the EuIG/GGG (110) maintains its hard axis of [001] through the temperature range, but within the easy (001) plane the lowest energy (easiest) direction changed from [110] to [$\bar{1}$10] as the temperature increased through T_{EPT}. For TmIG/GGG (110), the IP easy axis remained along [001] but the hardest direction in the (001) hard plane changed from [$\bar{1}$10] to [110] as the temperature increased through T_{HPT}. At the (thickness-dependent) transition temperatures, an ideal OOP easy-plane landscape is stabilized for EuIG, and an ideal OOP hard-plane is stabilized for TmIG. At these transition temperatures, the only anisotropy in the EuIG easy plane is the magnetocrystalline anisotropy, $\frac{K_{1,EuIG}}{4}$, and the only anisotropy in the TmIG hard plane is $\frac{K_{1,TmIG}}{4}$, where $K_{1,EuIG} = -3.8$ kJ/m^3 and $K_{1,TmIG} = -0.58$ kJ m^{-3} at 300 K,[50] both of which decrease in magnitude with increasing temperature.

Since the saturation magnetization M_s also changes with temperature T, we performed temperature-dependent VSM to extract M_s over the temperature range of interest (Note S4, Supporting Information). M_s versus T was fitted with a straight line and the M_s used for the anisotropy calculation was interpolated from the fit. We extracted the temperature dependence of anisotropies by assuming a linear dependence over the measurement

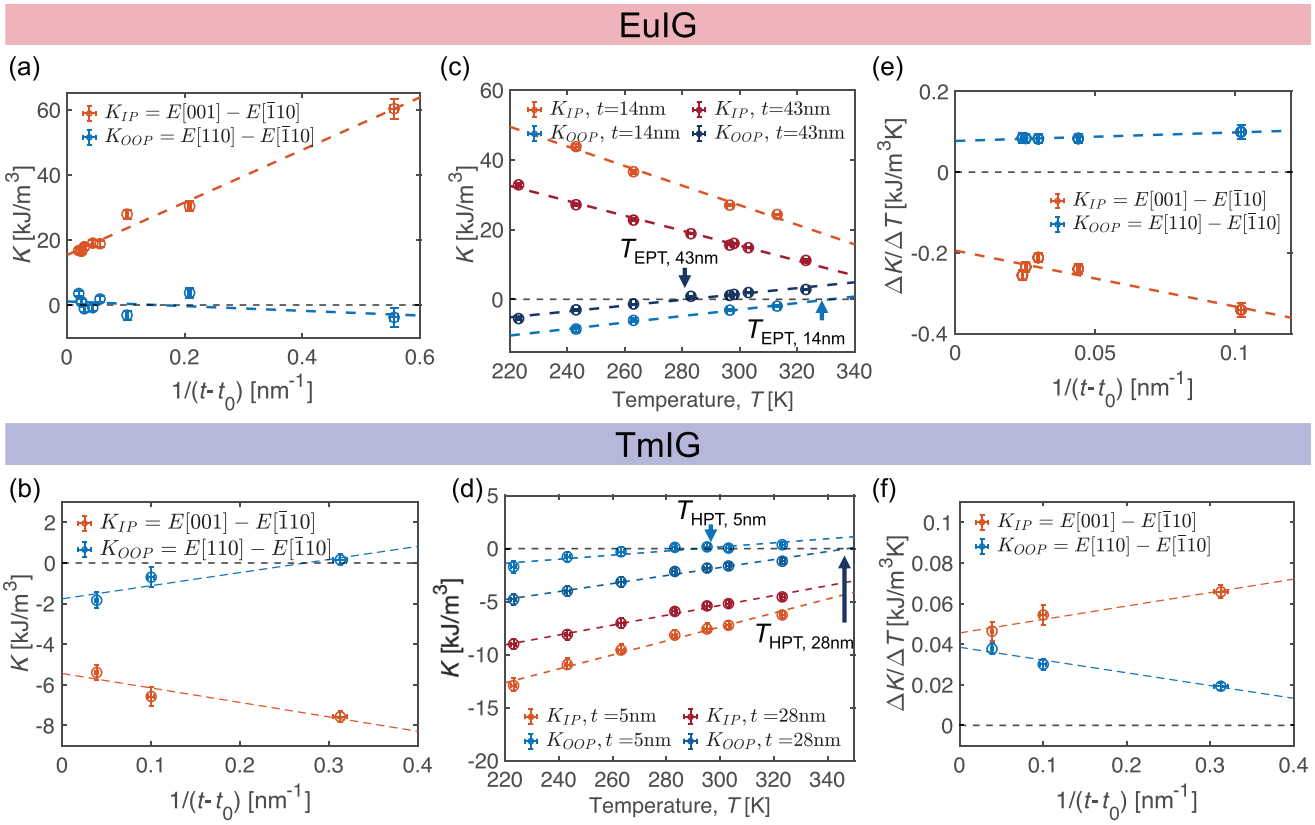

Figure 4. Anisotropy energies extracted from SMR measurements for Pt/EuIG/GGG (110) (top) and Pt/TmIG/GGG (110) (bottom). a,b) Room-temperature IP and OOP anisotropy energy K_{IP} and K_{OOP} for films of different thickness t (EuIG: t = 5, 8, 13, 21, 26, 37, 43, 45, 53 nm, t_0 = 2.9 nm; TmIG: t = 5, 12, 28, t_0 = 2.0 nm). c,d) Examples of the monotonic temperature dependence of the extracted anisotropy values for a thin and thick film. A transition in the easiest (hardest) anisotropy axis is observed in EuIG (TmIG) at T_{EPT} (T_{HPT}). At the transition temperature, an ideal OPEP (OPHP) is stabilized with only magnetocrystalline anisotropy $K_1/4$ in the plane. e,f) Temperature dependence of the anisotropies ($\Delta K/\Delta T$) as a function of film thickness to extract the temperature dependence of the bulk and surface anisotropies.

temperature range. From the plot of $\Delta K/\Delta T$ against $1/(t - t_0)$ in Figure 4e,f, we obtained the temperature dependence of the bulk and surface anisotropies for Pt/EuIG/GGG and Pt/TmIG/GGG, respectively.

Figure 5a shows a side-by-side comparison of the extracted anisotropy energies of EuIG, TmIG, and YIG (complete data for YIG is included in Note S6, Supporting Information). The results indicate the presence of surface anisotropy which has both IP and OOP contributions. The surface anisotropy includes contributions from both the film-substrate interface and the film-Pt interface. Both interfaces are 2-fold symmetric and the structural symmetry breaking contributes to both IP and OOP surface anisotropy terms through the Néel surface model.

Both EuIG and TmIG show a large IP surface anisotropy, in contrast to a negligible IP surface anisotropy in YIG, while YIG shows a larger OOP surface anisotropy compared to EuIG and TmIG. The IP surface anisotropy is more substantial in EuIG than in TmIG which could be related to a larger magnetoelastic coefficient and lattice mismatch strain in EuIG. Negligible surface and bulk IP anisotropies are measured in YIG since both SOC and lattice mismatch strain are negligible (a_{YIG} = a_{GGG} = 12.376 Å). Although a weak IP anisotropy could be present, it is in the J/m^3 range which is orders of magnitude smaller compared to other terms[51] and hence not discussed here.

We can consider YIG as a control dataset to disentangle the effect of Rashba SOC resulting from the Pt layer. Rashba SOC has a different symmetry compared to the Néel surface anisotropy, specifically, it induces an OOP surface anisotropy with no component in the film plane.[52,53] In the thickness series of YIG, we observed a large OOP surface anisotropy and negligible IP surface anisotropy, which agrees with the symmetry of Rashba SOC-induced surface anisotropy. Our Pt/YIG/GGG (110) films yielded an OOP surface anisotropy of 0.035 mJ m^{-2} which matches well with the previously reported value for Rashba SOC-induced interfacial anisotropy in Pt/BiYIG/GSGG (111) films.[53] According to Equation (3), the OOP Néel surface anisotropy exists for a simple cubic structure only when the lattice mismatch strain is nonzero. We hypothesize that the Néel surface anisotropy in YIG is negligible because of the negligible lattice mismatch, and Rashba SOC from Pt dominantly contributes to the surface anisotropy in YIG. Conversely, both Néel surface anisotropy and Rashba SOC contribute to EuIG and TmIG. Given Y^{3+} is not a magnetic ion and has negligible SOC, the Néel surface anisotropy could be strongly correlated to the SOC strength of the rare-earth element in the garnet thin film. The Rashba SOC effects in EuIG and TmIG are

Table 1. Extracted bulk and surface anisotropies for EuIG, TmIG, and YIG, with the bulk contribution to IP (OOP) anisotropy energy density, $K_{IP(OOP),\ bulk}$ and the surface contribution to IP (OOP) anisotropy energy density, $K_{IP(OOP),\ surface}$. The volume density, $K_{IP(OOP),\ surface}$ was converted from an area density, $E_{IP(OOP),\ surface}$ with the approximation of $h = a(1 + e_{33})\sqrt{2}$, where h is the thickness of the layer contributing to surface anisotropy and a is the lattice parameter, $h_{EuIG} = 1.78$ nm, $h_{TmIG} = 1.74$ nm and $h_{YIG} = 1.75$ nm. The magnetostatic contribution, $K_{MS} = \frac{1}{2}\mu_0 M_s^2$, is subtracted from $K_{OOP,\ bulk}$.

	$K_{IP,bulk}$ [kJ/m^3]	$K_{OOP,bulk} - K_{MS}$ [kJ/m^3]	$E_{IP,\ surface}$ [µJ/m^2]	$K_{IP,\ surface}$ [kJ/m^3]	$E_{OOP,\ surface}$ [µJ/m^2]	$K_{OOP,\ surface}$ [kJ/m^3]
EuIG	15.3 ± 0.8	− 2.6 ± 1.0	81 ± 4	45 ± 2	− 7 ± 5	− 4 ± 3
TmIG	− 5.4 ± 0.6	− 7.8 ± 0.5	− 6 ± 3	− 3.7 ± 1.7	6 ± 2	3.4 ± 1.4
YIG	0.0 ± 0.5	1.2 ± 0.4	0 ± 1	0.0 ± 0.5	35 ± 2	20 ± 1

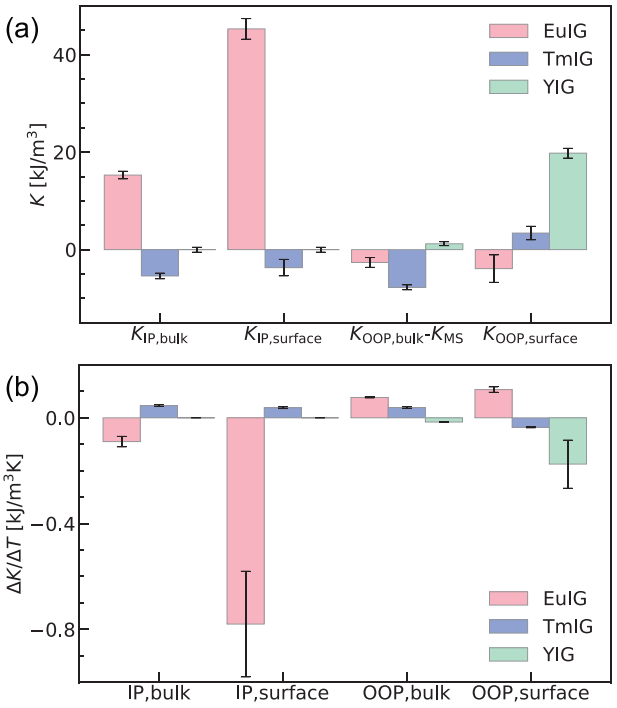

Figure 5. Summary plot of extracted anisotropies and their temperature dependence. a) Comparison of the extracted bulk and surface anisotropies for EuIG, TmIG, and YIG, with $K_{IP(OOP),\ bulk}$ the bulk contribution to IP (OOP) anisotropy energy density, $K_{IP(OOP),\ surface}$ the surface contribution to IP (OOP) anisotropy energy density converted from an areal density to volume density with the assumption of $h = a(1 + e_{33})\sqrt{2}$, where h is the thickness of the layer contributing to surface anisotropy and a is the lattice parameter. $h_{EuIG} = 1.78$ nm, $h_{TmIG} = 1.74$ nm, and $h_{YIG} = 1.75$ nm. $K_{OOP,bulk} - K_{MS}$ is plotted to remove the effect of demagnetization field in a thin film which contributes to the magnetostatic anisotropy K_{MS}. b) Comparison of the extracted temperature dependence $\Delta K/\Delta T$ of the bulk and surface anisotropies for EuIG, TmIG, and YIG.

expected to be on the same order of magnitude as in YIG due to their similar origin from the Pt overlayer. Therefore, we propose that Néel surface anisotropy contributes with a sign opposite to the Rashba SOC in both EuIG and TmIG and cancels most of the Rashba SOC surface anisotropy.

Surface anisotropy decreases with increasing temperature (Figure 5b), consistent with the Néel surface anisotropy model. This is reflected by a change in sign between the anisotropy energies at room temperature and their temperature dependence ($\Delta K/\Delta T$). Both the bulk and surface anisotropy have a negative temperature coefficient, consistent with the consideration of Néel surface anisotropy where the interaction energies between pairs of atoms and the magnetization decrease in strength with weaker SOC at elevated temperatures.[12] Previous work on the temperature dependence of surface anisotropy in metallic systems showed the same trend.[54]

Finally, we discuss other possible origins of the observed surface anisotropy. If surface anisotropy is dominated by strain relaxation in the surface layer of atoms, the surface anisotropy will contribute to lowering the total anisotropy energy for thinner films compared to thicker ones. However, an increase in anisotropy energy is observed in thinner films which contradicts

this hypothesis. RSM and rocking curve measurements also did not support a thickness dependence of the strain state. Furthermore, atom probe tomography of a TmIG film showed that the Tm:Fe composition ratio did not vary with depth (Note S1, Supporting Information). If the assumption for a constant M_s for all thicknesses is invalid, i.e., instead of a magnetic dead layer, the M_s is smaller in thinner films due to, e.g., point defects or interdiffusion, the total anisotropy energies calculated using the M_s from VSM would be approximately the same for all film thicknesses. However, this requires the single-ion anisotropy constant to be higher for thinner films which is implausible.

We therefore propose that there is a significant Néel surface anisotropy in our Pt/REIG/GGG. Despite the large number of atoms within a REIG unit cell and the complex crystal structure, there exists a lowest energy surface that dominates the nucleation and growth during film deposition, consistent with the sub-unit cell layer-by-layer growth of YIG observed by reflection high energy electron diffraction.[55,56] From the crystal structure, there are four types of distinguishable surface terminations in a REIG with (110) orientation, and our DFT calculations revealed that the surface configuration shown in Figure 1c,d has the lowest energy. This surface preserves RE-O bonds, and only the lower energy Fe-O bonds are broken (Note S6, Supporting Information). With the lowest energy surface being the dominant termination after film deposition, we can account for the consistency of the surface anisotropy measured across samples.

4. Discussion

We demonstrated that the inversion symmetry breaking at the (110) surface of an epitaxial complex oxide thin film can result in a surface contribution to the IP anisotropy, which can be explained by the phenomenological Néel surface model. Significant IP surface anisotropy is observed in heterostructures of two different REIGs, Pt/EuIG/GGG and Pt/TmIG/GGG, in contrast to negligible IP surface anisotropy in Pt/YIG/GGG, where the SOC strength and strain are negligible compared to those of EuIG and TmIG. However, the OOP surface anisotropy is complicated by the Rashba–induced isotropic IP anisotropy introduced by the heavy metal (Pt) overlayer which was required for SMR measurement. With the dataset for YIG as the control, we infer that the contribution from the Néel surface anisotropy is opposite to the Rashba contribution from Pt. Future work could characterize the surface anisotropy with bare films using angle-dependent ferromagnetic resonance measurements to deconvolve the contributions.

The variety of anisotropy landscapes tunable through thickness and temperature provide platforms for the exploration of dynamics and devices unprecedented in a simple uniaxial anisotropy system. Novel phenomena of exchange-driven autooscillation in the terahertz regime and coherent magnon transport through spin superfluidity have been proposed in systems with an OPEP anisotropy landscape.[22–25,57] More efficient IP switching has been predicted in systems with an OPHP anisotropy landscape.[26] The substantial IP surface anisotropy gives rise to a stronger easy plane anisotropy for Pt/EuIG/GGG and hard plane anisotropy for Pt/TmIG/GGG as the film becomes thinner, which makes them suitable candidates for these applications.

5. Experimental Section

Sample Preparation and Characterization: The EuIG, TmIG, and YIG thin films were grown on GGG (110) substrates (MTI Corporation) by PLD with a 248 nm wavelength KrF excimer laser at an energy of 350 mJ and a repetition rate of 5 Hz using a thickness-to-shot calibration of 50 nm per 10k shots. The targets were commercially available EuIG, TmIG, and YIG sintered disks with a 99.99% elemental purity. The growth atmosphere was oxygen at 150 mTorr with a base pressure of 5×10^{-6} Torr and the substrate temperature was 750 °C. HR-XRD measurements of the (440) reflection were performed on a Bruker D8 HR-XRD and the data was fitted to determine the film thickness and the strain from the (110) plane spacing. RMS measurements were performed on a Rigaku Smartlab X-ray diffractometer to map the IP and OOP lattice spacing. The saturation magnetization was determined using VSM. Assuming a dead (low magnetization) layer (t_0), caused for example by the interdiffusion of Ga and Fe atoms between the substrate and the film, the bulk saturation magnetization $M_{s,0}$ and magnetic dead layer t_0 were determined by plotting $M_s t$ against t, i.e., fitting to Equation M1. This agrees with a previously reported dead layer of 1.4 nm in TmIG grown on a GGG (111) substrate under similar conditions.[12]

$$M_s t = M_{s,0}\ (t - t_0) \tag{6}$$

SMR Measurements: 4 nm Pt was sputtered on EuIG (t nm)/GGG (110), TmIG (t nm)/GGG (110), and YIG (t nm)/GGG (110) from a 1 inch Pt target using a d.c. sputter system with an Ar pressure of 3 mTorr and base pressure of 5×10^{-8} Torr. Hall crosses with a typical active area dimension of 100 × 100 µm were patterned using standard photolithography and ion milling. The current arm of the device was aligned to 45 degrees from the IP principal anisotropy axes to maximize the signal.[45–47] Ta (6)/Au (150) contacts were patterned through lift-off.

SMR measurements were performed on a custom-built transport measurement setup at room temperature for Figure 3a,b. Temperature-dependence measurements were performed on the same setup including with cryogenic control and the temperature being read from a thermocouple mounted on the sample holder. The current was applied through an SR830 lock-in amplifier at a frequency of 9.973 kHz and a voltage amplitude of 5 V. A 10 kΩ resistor was connected in series with the device (with a typical resistance <100 Ω) to provide a stable current source of 0.5 mA. The transverse voltage was measured through the lock-in amplifier. The transverse magnetoresistance can be expressed in Equation M2, where $\phi_I = 45°$.

$$R_H = R_{SMR,AHE}\ \cos\theta + R_{SMR}\sin^2\theta \sin 2(\phi - \phi_I) + R_{OHE}\mu_0 H_3 \tag{7}$$

The anisotropy energies were obtained by fitting the SMR data with a macrospin model to minimize the total energy in the presence of an applied field and an anisotropy field. The detailed fitting protocols are discussed in Note S2 (Supporting Information). Discussion on the magnetization reversal behavior in EuIG with an OPEP anisotropy landscape can be found in our previous work.[45]

Statistical Analysis: Statistical analysis of data was carried out using Matlab software and Python packages through least-squares fit. Anisotropy energy values were obtained by fitting to SMR curves, which typically contain 100 data points in each scan. For extraction of bulk and surface anisotropy energies, all data points used for fitting were plotted, and the error bars were obtained from the covariance of the linear fit. Further error analysis associated with specific measurements can be found in the Supporting Information.

Supporting Information

Supporting Information is available from the Wiley Online Library or from the author.

Acknowledgements

Y.S. was supported by the NSF ECCS 1954606, DMR 2232380, and a Chyn Duoq Shiah Fellowship. The authors acknowledge Prof. Luqiao Liu for sharing the ion-milling facility. Characterization was performed in part in MIT Materials Research Laboratory shared facilities supported by the MRSEC Program DMR1419807. Nanofabrication was performed at the MIT.nano Facilities.

Conflict of Interest

The authors declare no conflict of interest.

Author contributions

Y.S. and K.L. contributed equally to this work. Y.S., G.S.D.B., and C.A.R. conceived the project. Y.S. and K.L. planned and conducted the experiments. Y.S. prepared the samples. H.T. performed DFT calculations. Y.S., K.L., H.T., G.S.D.B., and C.A.R. analyzed the data and wrote the manuscript. all authors contributed to the discussion of the data in the manuscript.

Data Availability Statement

The data that support the findings of this study are available in the supplementary material of this article.

Keywords

anisotropy, ferrimagnetic oxides, spintronics, surface and interfaces, thin films

Received: September 9, 2024
Revised: October 7, 2024
Published online: October 21, 2024

[1] S. Ikeda, K. Miura, H. Yamamoto, K. Mizunuma, H. D. Gan, M. Endo, S. Kanai, J. Hayakawa, F. Matsukura, H. Ohno, *Nat. Mater.* **2010**, *9*, 721.
[2] B. Dieny, M. Chshiev, *Rev. Mod. Phys.* **2017**, *89*, 025008.
[3] S. Parkin, S.-H. Yang, *Nat. Nanotechnol.* **2015**, *10*, 195.
[4] S. I. Kiselev, J. C. Sankey, I. N. Krivorotov, N. C. Emley, R. J. Schoelkopf, R. A. Buhrman, D. C. Ralph, *Nature* **2003**, *425*, 380.
[5] M. Krawczyk, D. Grundler, *J. Phys.: Condens. Matter* **2014**, *26*, 123202.
[6] M. Bibes, A. Barthelemy, *IEEE Trans. Electron Devices* **2007**, *54*, 1003.
[7] F. Trier, P. Noël, J.-V. Kim, J.-P. Attané, L. Vila, M. Bibes, *Nat. Rev. Mater.* **2021**, *7*, 258.
[8] R. Cheng, M. W. Daniels, J.-G. Zhu, D.i. Xiao, *Phys. Rev. B* **2015**, *91*, 064423.
[9] A. Stupakiewicz, C. S. Davies, K. Szerenos, D. Afanasiev, K. S. Rabinovich, A. V. Boris, A. Caviglia, A. V. Kimel, A. Kirilyuk, *Nat. Phys.* **2021**, *17*, 489.
[10] L. J. Cornelissen, J. Liu, R. A. Duine, J. B. Youssef, B. J. van Wees, *Nat. Phys.* **2015**, *11*, 1022.
[11] R. Timalsina, H. Wang, B. Giri, A. Erickson, X. Xu, A. Laraoui, *Adv. Electron. Mater.* **2024**, *10*, 2300648.
[12] L. Caretta, E. Rosenberg, F. Büttner, T. Fakhrul, P. Gargiani, M. Valvidares, Z. Chen, P. Reddy, D. A. Muller, C. A. Ross, G. S. D. Beach, *Nat. Commun.* **2020**, *11*, 1090.
[13] S. Vélez, S. Ruiz-Gómez, J. Schaab, E. Gradauskaite, M. S. Wörnle, P. Welter, B. J. Jacot, C. L. Degen, M. Trassin, M. Fiebig, P. Gambardella, *Nat. Nanotechnol.* **2022**, *17*, 834.
[14] S. Ding, A. Ross, D. Go, L. Baldrati, Z. Ren, F. Freimuth, S. Becker, F. Kammerbauer, J. Yang, G. Jakob, Y. Mokrousov, M. Kläui, *Phys. Rev. Lett.* **2020**, *125*, 177201.
[15] A. Quindeau, C. O. Avci, W. Liu, C. Sun, M. Mann, A. S. Tang, M. C. Onbasli, D. Bono, P. M. Voyles, Y. Xu, J. Robinson, G. S. D. Beach, C. A. Ross, *Adv. Electron. Mater.* **2017**, *3*, 1600376.
[16] E. R. Rosenberg, L. S. Beran, C. O. Avci, C. Zeledon, B. Song, C. Gonzalez-Fuentes, J. Mendil, P. Gambardella, M. Veis, C. Garcia, G. S. D. Beach, C. A. Ross, *Phys. Rev. Mater.* **2018**, *2*, 094405.
[17] L. Soumah, N. Beaulieu, L. Qassym, C. Carrétéro, E. Jacquet, R. Lebourgeois, J. Ben Youssef, P. Bortolotti, V. Cros, A. Anane, *Nat. Commun.* **2018**, *9*, 3355.
[18] C. O. Avci, A. Quindeau, C.-F. Pai, M. Mann, L. Caretta, A. S. Tang, M. C. Onbasli, C. A. Ross, G. S. D. Beach, *Nat. Mater.* **2017**, *16*, 309.
[19] L. Caretta, S.e-H. Oh, T. Fakhrul, D.-K. Lee, B. H. Lee, S.e K. Kim, C. A. Ross, K.-J. Lee, G. S. D. Beach, *Science* **2020**, *370*, 1438.
[20] J. F. Nye, *Physical Properties Of Crystals: Their Representation By Tensors And Matrices*, Oxford University Press, Oxford, United Kingdom, **1984**.
[21] M. Hoffmann, B. Zimmermann, G. P. Müller, D. Schürhoff, N. S. Kiselev, C. Melcher, S. Blügel, *Nat. Commun.* **2017**, *8*, 308.
[22] O. R. Sulymenko, O. V. Prokopenko, V. S. Tiberkevich, A. N. Slavin, B. A. Ivanov, R. S. Khymyn, *Phys. Rev. Appl.* **2017**, *8*, 064007.
[23] R. Cheng, D. Xiao, A. Brataas, *Phys. Rev. Lett.* **2016**, *116*, 207603.
[24] D. Marković, M. W. Daniels, P. Sethi, A. D. Kent, M. D. Stiles, J. Grollier, *Phys. Rev. B* **2022**, *105*, 014411.
[25] E. A. Montoya, A. Khan, C. Safranski, A. Smith, I. N. Krivorotov, *Commun. Phys.* **2023**, *6*, 184.
[26] Y. Zhou, C. Guo, C. Wan, X. Chen, X. Zhou, R. Zhang, Y. Gu, R. Chen, H. Wu, X. Han, F. Pan, C. Song, *Phys. Rev. Appl.* **2020**, *13*, 064051.
[27] H. Lüth, *Surfaces and Interfaces of Solid Materials*, Springer, Berlin Heidelberg, **1995**.
[28] W. Mönch, *Semiconductor Surfaces and Interfaces*, Springer, Berlin Heidelberg, **2001**.
[29] L. Néel, *Comptes Rendus Hebdomadaires Des Seances De L Academie Des Sciences* **1953**, *237*, 1468.
[30] M. T. Johnson, R. Jungblut, P. J. Kelly, F. J. A. den Broeder, *J. Magn. Magn. Mater.* **1995**, *148*, 118.
[31] S. Monso, B. Rodmacq, S. Auffret, G. Casali, F. Fettar, B. Gilles, B. Dieny, P. Boyer, *Appl. Phys. Lett.* **2002**, *80*, 4157.
[32] D. S. Chuang, C. A. Ballentine, R. C. O'Handley, *Phys. Rev. B* **1994**, *49*, 15084.
[33] R. H. Victora, J. M. MacLaren, *Phys. Rev. B* **1993**, *47*, 11583.
[34] U. Gradmann, J. Korecki, G. Waller, *Applied Physics A Solids and Surfaces* **1986**, *39*, 101.
[35] C. Chappert, P. Bruno, *J. Appl. Phys.* **1988**, *64*, 5736.
[36] G. F. Dionne, *Magnetic Oxides*, Springer, Berlin, Germany, **2009**.
[37] R. Zeller, *Computational Nanoscience* **2006**, *31*, 74419.
[38] G. Kresse, D. Joubert, *Phys. Rev. B* **1999**, *59*, 1758.
[39] G. Kresse, J. Furthmüller, *Phys. Rev. B* **1996**, *54*, 11169.
[40] J. P. Perdew, K. Burke, M. Ernzerhof, *Phys. Rev. Lett.* **1996**, *77*, 3865.
[41] H. J. Monkhorst, J. D. Pack, *Phys. Rev. B* **1976**, *13*, 5188.
[42] A. H. Eschenfelder, *Magnetic Bubble Technology*, Springer, Berlin Heidelberg, **1980**.
[43] E. Rosenberg, J. Bauer, E. Cho, A. Kumar, J. Pelliciari, C. A. Occhialini, S. Ning, A. Kaczmarek, R. Rosenberg, J. W. Freeland, Y. Chen, J. Wang, J. LeBeau, R. Comin, F. M. F. De Groot, C. A. Ross, *Small* **2023**, *19*, 2300824.

[44] J. J. Bauer, P. Quarterman, A. J. Grutter, B. Khurana, S. Kundu, K. A. Mkhoyan, J. A. Borchers, C. A. Ross, *Phys. Rev. B* **2021**, *104*, 094403.
[45] Y. Song, A. C. Kaczmarek, G. S. D. Beach, C. A. Ross, *Phys. Rev. Mater.* **2023**, *7*, 084407.
[46] Y.-T. Chen, S. Takahashi, H. Nakayama, M. Althammer, S. T. B. Goennenwein, E. Saitoh, G. E. W. Bauer, *Phys. Rev. B* **2013**, *87*, 144411.
[47] H. Nakayama, M. Althammer, Y.-T. Chen, K. Uchida, Y. Kajiwara, D. Kikuchi, T. Ohtani, S. Geprägs, M. Opel, S. Takahashi, R. Gross, G. E. W. Bauer, S. T. B. Goennenwein, E. Saitoh, *Phys. Rev. Lett.* **2013**, *110*, 206601.
[48] H. Callen, *Appl. Phys. Lett.* **1971**, *18*, 311.
[49] A. C. Kaczmarek, E. R. Rosenberg, Y. Song, K. Ye, G. A. Winter, A. N. Penn, R. Gomez-Bombarelli, G. S. D. Beach, C. A. Ross, *Nat. Commun.* **2024**, *15*, 5083.
[50] S. M. Zanjani, M. C. Onbaşlı, *Data in Brief* **2020**, *28*, 104937.
[51] J. Mendil, M. Trassin, Q. Bu, J. Schaab, M. Baumgartner, C. Murer, P. T. Dao, J. Vijayakumar, D. Bracher, C. Bouillet, C. A. F. Vaz, M. Fiebig, P. Gambardella, *Phys. Rev. Mater.* **2019**, *3*, 034403.
[52] A. J. Lee, A. S. Ahmed, B. A. McCullian, S. Guo, M. Zhu, S. Yu, P. M. Woodward, J. Hwang, P. C. Hammel, F. Yang, *Phys. Rev. Lett.* **2020**, *124*, 257202.
[53] B. H. Lee, T. Fakhrul, C. A. Ross, G. S. D. Beach, *Phys. Rev. Lett.* **2023**, *130*, 126703.
[54] M. Farle, W. Platow, A. N. Anisimov, B. Schulz, K. Baberschke, *J. Magn. Magn. Mater.* **1997**, *165*, 74.
[55] C. Tang, M. Aldosary, Z. Jiang, H. Chang, B. Madon, K. Chan, M. Wu, J. E. Garay, J. Shi, *Appl. Phys. Lett.* **2016**, *108*, 102403.
[56] Y. Krockenberger, K.-S. Yun, T. Hatano, S. Arisawa, M. Kawasaki, Y. Tokura, *J. Appl. Phys.* **2009**, *106*, 123911.
[57] S. o Takei, Y. Tserkovnyak, *Phys. Rev. Lett.* **2014**, *112*, 227201.